Research Paper
J. Astron. Space Sci. 42(4), 85-96 (2025)
https://doi.org/10.5140/JASS.2025.42.4.85

JASS Journal of Astronomy and Space Sciences

Episodic Mass Wasting and Exposure of High Reflectance Material Within the Shackleton Crater Permanently Shadowed Region

Prasun Mahanti[1†], Shuai Li[2], Mark S. Robinson[1], Thomas Watters[3], Paul Lucey[2], Brad Jolliff[4], Madeleine Manheim[1], Cordell Michaud[1]

[1]Intuitive Machines, Phoenix, Arizona, AZ 85004, USA
[2]Hawaii Institute of Geophysics and Planetology, University of Hawaii, Honolulu, HI 96822, USA
[3]Smithsonian Institution, Washington, DC 20024, USA
[4]Department of Earth, Environmental, and Planetary Sciences, Washington University, St. Louis, MO 63130, USA

The Shackleton crater permanently shadowed region (PSR) exhibits high 1,064 nm reflectance and S-band radar circular polarization ratios (CPR), which previous studies interpreted as indicating the presence of water-ice or frost. In the absence of photogeologic evidence, alternative hypotheses offered for the reflective properties of the Shackleton crater PSR (mass wasting, presence of pure anorthosite, and interior blockiness) were not confirmed. ShadowCam has acquired high signal-to-noise ratio stereo images of Shackleton crater; we use these images, derived digital terrain models, and M^3 data to show that episodic mass wasting is active inside Shackleton, arising from the instability of steep wall slopes. We conclude that the relatively high reflectance within the Shackleton PSR results from continued exposure of plagioclase-rich material and not from water-ice or frost. In addition, mass wasting also excavates small blocks that collect on the wall and floor, mainly responsible for the enhanced radar CPR signature.

Keywords: ShadowCam, permanently shadowed region, shackleton crater, crystalline plagioclase, mass wasting

1. INTRODUCTION

Considering its reported age [> 3.4 Ga (Spudis et al. 2008; Zuber et al. 2012; Tye et al. 2015; Kring et al. 2021), ~2.5 Ga (Giuri et al. 2024)], Shackleton crater (20 km diameter) is a well-preserved simple bowl-shaped crater. Lunar orbiter laser altimeter (LOLA) topography (Zuber et al. 2012) indicates steep walls (> 30°) uncharacteristic of craters of early Imbrian and older ages (Kreslavsky & Head 2016). Alternatively, larger younger craters (Copernican and Eratosthenian) exhibit steeper wall slopes and extensive mass wasting features (Xiao et al. 2013; Kokelaar et al. 2017; Watters et al. 2022). However, the interior walls of Shackleton crater show no clear evidence of large-scale wall slumping or regolith flow and appear smooth from the available LOLA topography. Downslope streamers of low-albedo regolith were identified (Gawronska et al. 2020) at directly illuminated rim sections Lunar Reconnaissance Orbiter Narrow Angle Camera (LROC NAC) images (Robinson et al. 2010), but since much of Shackleton crater is within a permanently shadowed region (PSR), such image analysis was not possible in the earlier work.

The South Pole-Aitken (SPA) basin formation event may have ejected and emplaced the primordial anorthositic layer in the south polar region. Shackleton crater formed on the rim of the SPA basin, implying that its pre-impact surface was primarily SPA ejecta, likely composed of ancient crustal material [primarily anorthosite (Ohtake et al. 2009)]. Spectral Profiler data from SELENE and LROC NAC photogeologic inference both suggest the presence of pure anorthosite on the sunlit portions of the crater rim and wall (Yamamoto et al. 2012; Gawronska et al. 2020). However,

Received 21 AUG 2025 **Revised** 24 SEP 2025 **Accepted** 26 SEP 2025
†**Corresponding Author**
Tel: +1-480-385-9241, E-mail: pmahanti@intuitivemachines.com
ORCID: https://orcid.org/0000-0003-0805-8074

https://janss.kr pISSN: 2093-5587 eISSN: 2093-1409

illumination is insufficient to allow spectral compositional determinations inside the PSR boundary, which starts 600 m to 1,400 m below Shackleton's rim.

The interior of Shackleton crater was suggested to contain water-ice from the bistatic radar experiments (Nozette et al. 1996) and from neutron spectroscopy measurements (Feldman et al. 2000). One hypothesis for the relatively high interior optical reflectance of Shackleton crater was the presence of up to 20% water-ice (Zuber et al. 2012). Competing hypotheses were suggested for the observed optical and radar reflectance properties (Simpson & Tyler 1999; Thomson et al. 2012; Zuber et al. 2012; Haruyama et al. 2013; Lucey et al. 2014); the absence of high-resolution surface images and topography hindered testing these interpretations.

Here, we bridge the knowledge gap with ShadowCam (Robinson et al. 2023) images enabled by secondary illumination. ShadowCam is an instrument onboard the Korean Pathfinder Lunar Orbiter (KPLO; also known as Danuri) designed to acquire high-resolution images at the PSRs to create maps for scientific analysis and exploration. From these images, we mapped the interior landforms within the Shackleton crater PSR and measured topographic slope from the ShadowCam digital terrain model (DTMs) to recognize modifications caused by mass wasting and characterized wall slope stability. Finally, we geo-localize pure anorthosite from the spectral identification of crystalline plagioclase within the directly sunlit portions of Shackleton crater and link them to ShadowCam observations of high radiance contrast outcrops.

2. DATA AND METHOD

2.1 Assessment of Slope - Horizontal Curvature and Wall Stability

Our analysis utilizes 2-m/pixel images acquired by ShadowCam and topography derived from ShadowCam stereo images (also see Appendix 1). Nine radiance ($Wm^{-2}sr^{-1}\mu m^{-1}$) calibrated stereo observations (Humm et al. 2023) were used to obtain a 12 m/px DTM of a pole-facing interior sector of Shackleton crater (Fig. 1(a)). Using the ShadowCam DTM of the interior wall of the Shackleton crater, we calculate the slope (Fig.1(b)), derive slope statistics and investigate the interior wall slope stability (Fig. 1(c)) with a factor of safety (F_s) analysis.

For an infinite-slope stability model (Watters et al. 2024), the factor-of-safety (F_s) describes the ratio of shear strength to shear stress for downslope movement (Newmark 1965; Gallen et al. 2015). The infinite-slope stability model considers surface slope (θ; bidirectional slope), angle of internal friction (ϕ; assumed to vary between 30° to 35°; Mitchell et al. 1972), cohesion (C), thickness (t) and bulk density ρ_r of the regolith layer. Here, we assume a bulk density of 1,660 kg/m^3 for the regolith (Mitchell et al. 1972; Carrier et al. 1991), and that the regolith has low cohesion (0.1 kPa; Mitchell et al. 1972). The minimum thickness of the regolith layer moving downslope is assumed to be about 1m, since recent regolith landslides observed in LROC NAC temporal images (Watters et al. 2022) do not form detectable detachment scarps (Watters et al. 2024).

In terms of the parameters, F_s is expressed as

$$F_s(\theta) = \frac{C}{\rho_r g t \sin(\theta)} + \frac{\tan(\phi)}{\tan(\theta)}$$

Of these parameters, regolith cohesion has the most significant influence on slope stability (Watters et al. 2024). We compute F_s for each cell in the partial DTM, and the entire crater interior from 60 m LOLA digital elevation model (DEM; Barker et al. 2021) since the ShadowCam DTM had limited coverage. A cell is deemed unstable if $F_s < 1$. A higher angle of friction can allow steeper slopes to be stable. The angle of friction, ϕ, was varied in our analysis to determine the maximum angle of friction for each cell.

Topographic signatures indicating erosional/mass-wasting features and downslope motion are found using horizontal curvature (K_h) maps computed in a direction perpendicular to the slope. K_h maps show the convergence and divergence (Krcho 1983; Shary et al. 2002) of flow across the interior wall surface. Positive, negative, and zero curvatures indicate whether the surface is convex (like ridges), concave (like channels), or flat.

2.2 Crystalline Plagioclase Abundance Map

To localize pure anorthosite, we utilized a crystalline plagioclase map (140 m/px; Li et al. 2025), which was derived from a controlled mosaic of thermally corrected (Li & Milliken 2016) and spatially registered M^3 data near the lunar south pole (see also Appendix 3). We applied integrated band depth (IBD) parameters to differentiate between various mineral and glassy components. Specifically, IBDs near 1 μm were used to detect pyroxene, olivine, and glasses, while plagioclase was assessed using IBDs near 1.25 μm. Pyroxene and spinel were identified based on IBD values near 2 μm. These band parameters are consistent with those reported in Cheek et al. (2013), and Hanna et al. (2014). Strong absorptions near 1.25 μm

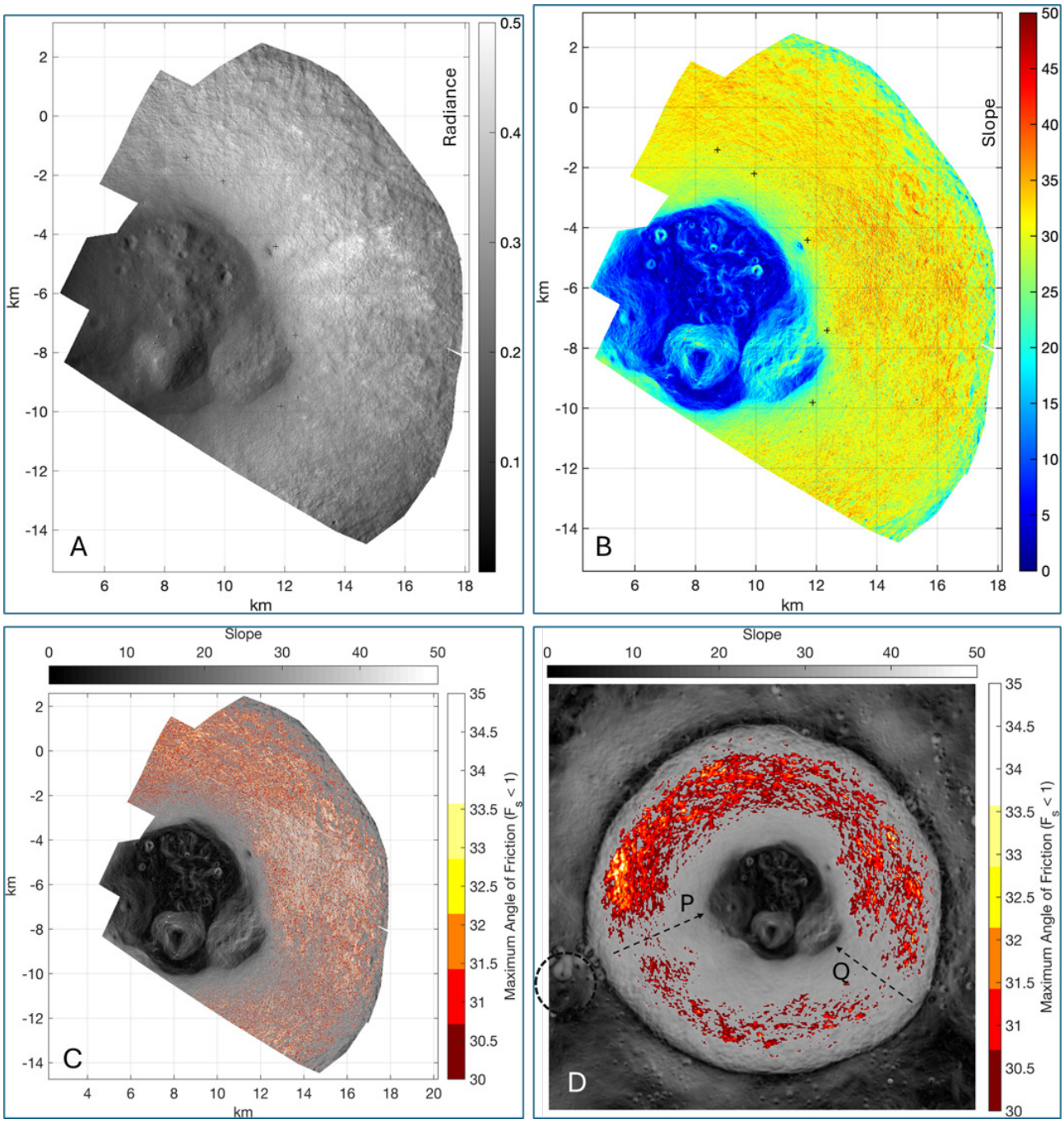

Fig. 1. ShadowCam stereo ortho-mosaic (a) revealing high reflectance 'bright' units ~1 km from the floor. (b) Shackleton slope map in polar stereographic projection. X and Y axis are distance in meters from south pole. Colorbar indicates bidirectional slope. Examples of locations of extreme high wall slopes (99th percentile) close to floor are marked with black '+' sign. Slope instability maps at Shackleton crater from (c) ShadowCam DTM's (12 m/px) and (d) LOLA DEM (60 m/px). Colors indicate the maximum angle of friction for stable slopes, indicating that most of these slopes (b) are unstable. The dashed black arrows show the possible landslide directions. DTM, digital terrain model; LOLA, lunar orbiter laser altimeter; DEM, digital elevation model.

indicate the presence of crystalline plagioclase, which exhibits higher reflectance compared to mafic components and mature regolith, resulting in significant contrast differences in radiance images.

3. RESULTS AND DISCUSSIONS

3.1 Episodic Mass Wasting Active inside Shackleton Crater

Shackleton crater is bowl-shaped with a depth-to-diameter

ratio of 0.195 ± 0.025 and a well-preserved rim crest typical of relatively fresh craters. Interior walls within the Shackleton PSR appear smooth at scales above 30 m, and ShadowCam images show relatively high reflectance outcrops. Interior slopes of permanently shadowed walls within our high-resolution map area (Fig. 1(b)) range from 23° (1st percentile) to 39° (99th percentile) with a median of 31°. The 90th, 95th, and 98th percentile slopes are 35°, 36° and 38°, respectively, all higher than the typical angle of repose for dry materials (Mitchell et al. 1972; Jaeger et al. 1989).

Previous studies indicate that slopes of 32° or steeper mostly occur in craters with ages younger than early Imbrian (Kreslavsky & Head 2016). In this study, we find that our conservative maximum slope values (99th percentile) are 39°, >10% higher than previously reported maximum values for Shackleton crater (35°, at 10 m baseline, Zuber et al. 2012). Additionally, approximately 9% of the permanently shadowed wall area has slopes greater than 35°. Further, our wall slope analysis of large craters (D > 5km) near the south pole reveals that Shackleton is one of the few craters within ten degrees of the south pole with such steepness of the interior walls.

Analysis of Shackleton wall slope stability (Watters et al. 2024) using a 468 m/px (LOLA; Barker et al. 2016) DTM suggests that most of the steep slopes in Shackleton crater are susceptible to regolith landslides. A similar analysis was conducted here for the entire Shackleton PSR wall area (Fig. 1(d)) using a 60 m/pixel LOLA DTM and for the ShadowCam DTM (12 m/pixel, Fig. 1(c)), corroborating this recent finding with additional details.

- Unstable slopes within PSR are larger than 32°, and occur from ~500 m below the rim up to a depth of ~2 to ~2.7 km below the rim (Fig.1 and Fig. A2 in Appendix 4).
- Approximately 30% of the wall area inside the PSR boundary has unstable slopes in both ShadowCam and LOLA DTMs.
- Slope instability is non-uniform and asymmetric. The far/bottom interior walls are more stable than the near/top interior walls. The most unstable region is (Fig. 1(d)) ~5 km away from the south pole (local median slope > 37°), at the leading rim (about 800 meters higher than the trailing rim). (Directionality descriptions in Appendix 2 and Fig. A1).
- The F_s maps show two stable zones (rim-floor direction) in the far/bottom interior walls. Wall slides that lead to the two slumps (Fig. 1(d), P and Q) at the wall-floor intersection may have removed outcrops, thus lowering wall instability here. Impacts near Shackleton's rim (–89.58, 198.00, e.g., dashed circle in Fig. 1(d)) were recently suggested as the cause for landslides leading to the floor mounds P and Q (Mitusov et al. 2023).
- Within the range of ϕ (30° to 35°) selected for analysis, the slopes estimated from ShadowCam DTM are stable if ϕ > 33°. Hence, we hypothesize that the angle of internal friction at Shackleton's interior walls must be less than 33° to support mass wasting.

Extreme high slopes and factor of safety computations from ShadowCam DTMs from this work indicate that mass wasting processes (falls, slides, slumps, flows, and creeps) should be active within Shackleton. Signatures of such processes can be found in (Xiao et al. 2013) for craters of Eratosthenian or Copernican age.

ShadowCam images and DTMs reveal evidence of episodic mass wasting within Shackleton crater. In PSRs, the diffuse nature and large phase angles of secondary illumination suppress reflectance contrast, making it difficult to identify subtle flowlines. However, some ShadowCam images (Fig. 2(a) and 2(b)) show these flow lines overlapped by block-fall tracks, indicating downslope movement. Flow lines and block tracks also form criss-cross patterns seen in ShadowCam images, expected from the inherent randomness of the block-fall pathways. ShadowCam images show examples that debris flows initiate above the PSR boundary (Fig. 2(c)) - similar to downslope streamers of low albedo regolith identified (Gawronska et al. 2020) in LROC NAC images near Shackleton's rim.

Topographic signatures of slope erosion can be observed in maps of horizontal curvature (K_h maps, Fig. 2(d)). The K_h maps reveal flow patterns caused by a cumulative erosional mechanism. The K_h maps show converging negative curvature striations in the rim-to-floor direction while forming crisscross patterns. Nearer to the rim, the K_h map patterns resemble similar patterns seen in ShadowCam images (Fig. 2(c)). Evidence of large-scale (> 100 m wide) flows and landslides that can dislodge large volumes of debris is not seen in ShadowCam images.

At the steep walls within PSRs, erosion [from impact shaking and endogenic seismic activity; (Mishra & Kumar 2022; Watters et al. 2024)] moves loose regolith and blocks downslope as debris flows. Only a few fresh small craters (D < 30 m) are observed on the crater walls because debris flows quickly erase small craters. Large median wall slopes without distinct signs of significant sliding events indicate that mass wasting mainly occurs as dry, sweeping, granular flows (Xiao et al. 2013) in the rim-to-floor direction. The downslope debris flow does not lead to deep channel formations and is more similar to narrow (< 20 m wide)

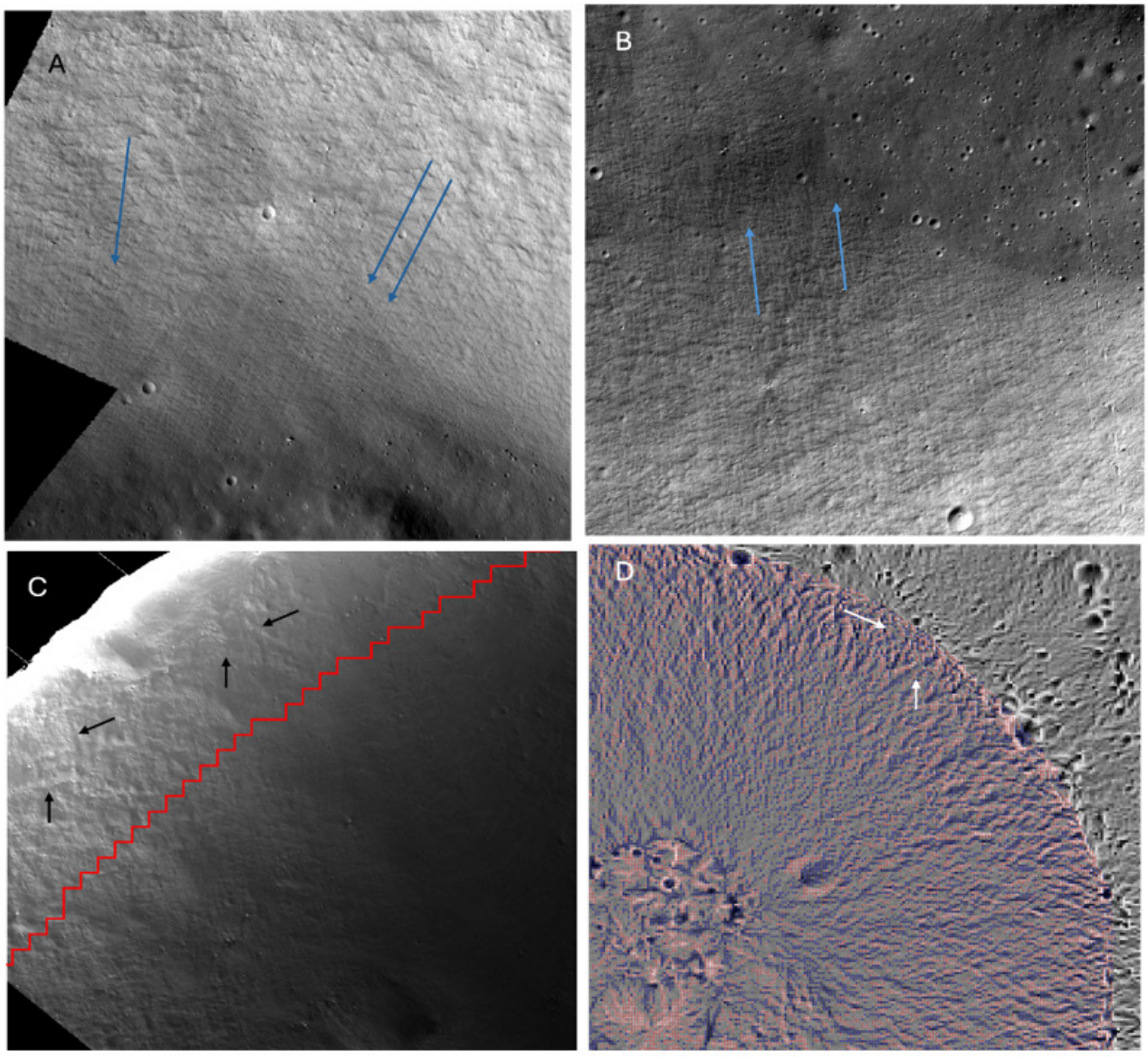

Fig. 2. ShadowCam images ((a) from stereo mosaic, (b) from image M084203041S) show the combined effect of flow lines and block tracks in the general rim-to-floor direction (blue arrows). Tracks and flow lines, visible in both the floor (with a darker contrast in the radiance image) and the wall regions (relatively brighter), overlap and cross each other. ShadowCam images ((c) from image M081161776S) also show signatures (black arrows) of downslope flow near the rim, where some of the flows originate. Similar signatures can be seen in the horizontal curvature (K_h) map computed from the lunar orbiter laser altimeter DTM (LOLA DTM) (d). Pixels within the K_h map and inside Shackleton's rim are colored based on curvature sign - blue pixels (negative curvature) represent local concavities, while red pixels (positive curvature) are locally convex. The local concavities merge and converge, transporting debris in the rim-to-floor direction. DTM, digital terrain model.

sweeping flows observed in Copernican/Eratosthenian craters, which move loose soil and block fragments (Xiao et al. 2013). Similar flow patterns are visible (Xiao et al. 2013; Kokelaar et al. 2017) in directly illuminated images of steep morphology elsewhere on the Moon (e.g., crater walls, volcanic pits and domes, mountainous elevations).

ShadowCam images show that the interior of Shackleton crater is peppered with blocks. Compounded with the distribution of steep, unstable slopes (Fig. 1) and the evidence of mass wasting flows (Fig. 2), these observations are consistent with a young age. Accordingly, we suggest that Shackleton is not of Imbrian age but is younger, at least mid-Eratosthenian (~2.5 Ga). A similar suggestion supporting an Eratosthenian age for Shackleton ejecta deposits was made recently (Giuri et al. 2024) from crater size frequency distribution analysis (CSFD), contrasting previous work (Spudis et al. 2008; Zuber et al. 2012; Tye et al. 2015; Kring et al. 2021) that estimates the age of Shackleton to be > 3.4 Ga.

3.2 Crystalline Plagioclase Exposures within Shackleton Crater

Previous work determined that the spectral identifications of pure anorthosite correspond to high albedo blocky exposures within the interior walls of Shackleton crater down to a depth of approximately 1 km (Yamamoto et al. 2012; Gawronska et al. 2020). Blocks in the Shackleton ejecta with similar albedo contrast were speculated (Gawronska et al. 2020) to be ejected blocks of purest (> 98% plagioclase) anorthosite (PAN; Ohtake et al. 2009). Here, we used the unique absorption near 1.25 μm in M^3 data to identify crystalline plagioclase exposures (Ohtake et al. 2009; Cheek et al. 2013; Cheek & Pieters 2014) in our map for pure (> 95% plagioclase) anorthosite detections.

ShadowCam observations of the Shackleton permanently shadowed walls show distinct high reflectance units as far as < 2 km below the rim (Fig. 2). Some ShadowCam observations also image the temporarily shadowed region (i.e., directly illuminated at other times) below the rim and show the high reflectance outcrops. Where available, overlaying the M^3 data over ShadowCam images (Fig. 3, temporarily shadowed areas) allows us to follow a spectral detection of crystalline plagioclase from the temporarily shadowed (for which M^3 data is also available when it was sunlit) region, associate the spectral signatures with the high reflectance outcrops, and then follow the high reflectance outcrops on the permanently shadowed wall towards the floor. Our analysis of the M^3 observations confirms that the high reflectance outcrops are consistent with crystalline plagioclase observed along the rim in primary illuminated areas.

Our M^3 maps (Li et al. 2025) show that crystalline plagioclase is present at Shackleton below the rim and outside the PSR. The plagioclase detections are extensive at the near/leading wall but less at the trailing wall (pole-facing), which is glass or pyroxene-rich and lower in plagioclase content. The two relatively stable zones discussed earlier (Section 3) have

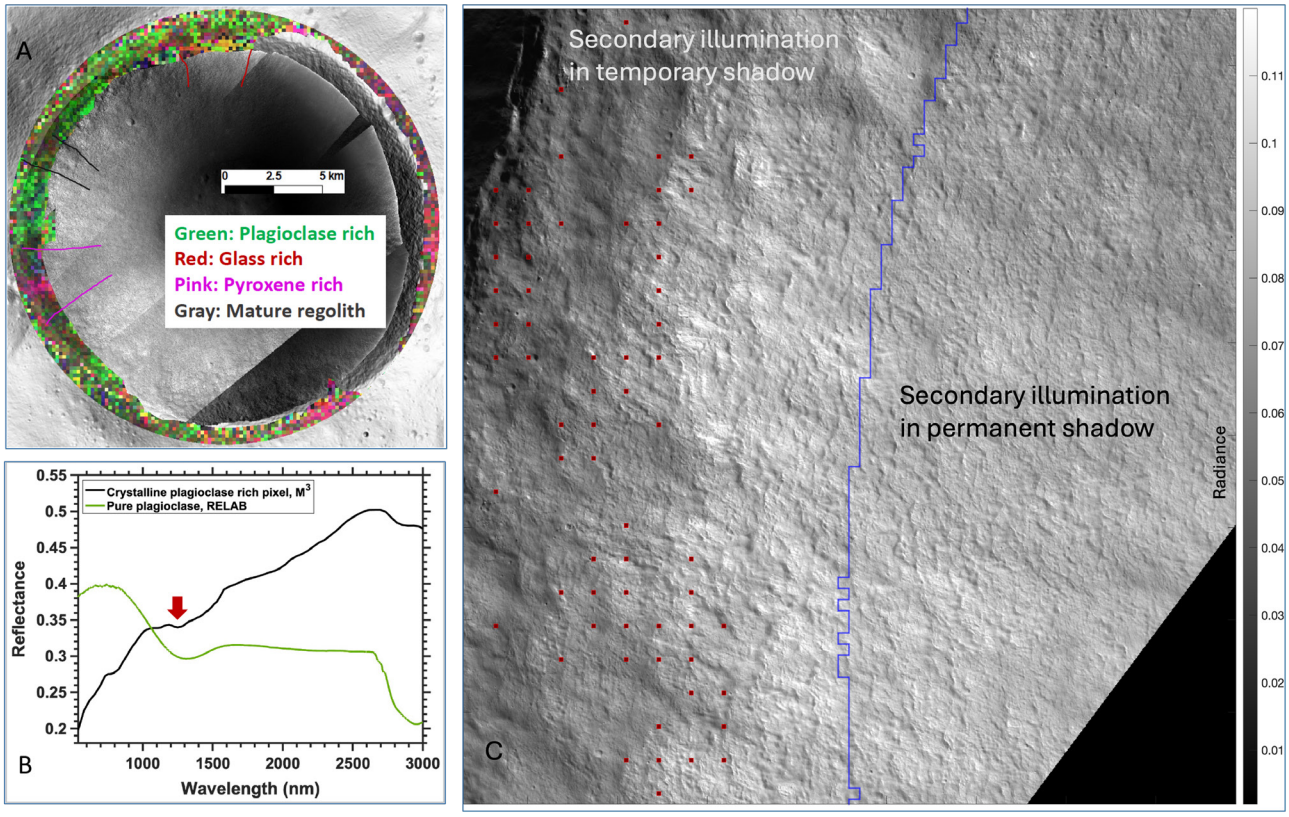

Fig. 3. Crystalline plagioclase at Shackleton crater. (a) Mineralogy derived from M^3 observations. Green pixels indicate plagioclase-rich regions. Colored lines drawn indicate locations of other mineralogy components (b) M^3 spectra of crystalline plagioclase-rich pixel on the rim of the crater (–89.822°S, –157.307°W). A spectrum of terrestrial pure, crystalline plagioclase is plotted to indicate the unique absorption near 1.25 μm seen (red arrow indicates center of the range) in terrestrial and lunar crystalline plagioclase. (c) ShadowCam image M014524048S of the leading wall (nearer to the south pole) of Shackleton, showing exposed high reflectance units. M^3 data (red dots) overlayed indicates crystalline plagioclase rich locations that also partially overlap bright PAN (purest anorthosite [≥ 98% plagioclase; (Ohtake et al. 2008)] exposure identified in earlier work (Yamamoto et al. 2012; Gawronska et al. 2020). Directionality descriptions are provided in Appendix 2 and Fig. A1. PAN, purest anorthosite.

a low density of outcrops and a muted plagioclase signature at the corresponding rim portions. Landslides removed the rim portions at these zones, smoothed the outcrops, and led to floor mounds.

The assessment of PAN based on the absorption near 1.25 μm also requires the measurement of mafic components, particularly pyroxene. Thus, we also examine absorptions near 1 μm and 2 μm to constrain the abundances of mafic minerals, which indicate purity (> 95% plagioclase). The absence of pronounced absorptions near either 1 μm or 2 μm indicates very low mafic (e.g., pyroxene) content (< 2%; Cheek et al. 2013), typical of pure anorthosite.

3.3 The High Albedo and Blockiness of Shackleton Crater Interior

The albedo of the interior is high for fresh craters of its size, though not uniquely so (Lucey et al. 2014). The presence of high albedo crystalline plagioclase, steep slopes that facilitate exposure of the high albedo material, and possibly reduced darkening of the exposed material from space weathering are responsible for the high wall albedo. While surface ice / frost was posed as an alternate explanation for the anomalously high reflectance in earlier work (Zuber et al. 2012), our analysis of over 200 ShadowCam images of the wall and floor does not reveal clear evidence of surface ice or frost. In the context of previous water frost detections within Shackleton crater (Li et al. 2018), if present, then such concentrations are low and do not result in identifiable signatures in ShadowCam images. Furthermore, if a higher concentration of water-ice was mixed with regolith, a significantly higher cohesion (Gertsch et al. 2006) would result, opposing the mass wasting evidenced in this work.

Shackleton's floor exhibits lower average radiance than the walls (Mahanti et al., 2023). A large part of the floor is occupied by landslide material that appears to superpose any possible original impact melt and ejecta fallback from crater formation. Over time, the floor material should have matured similarly as the ejecta albedo outside the rim. However, the continuous admixing of debris from the wall elevates the average albedo of the floor, compared to other south polar surrounding craters. Coupled with reduced darkening from space weathering within PSRs, this is a probable reason for the elevated floor albedo of Shackleton (Lucey et al. 2014). Continuous mass wasting processes at the walls dislodge blocks that contribute blocks now visible on the wall and floor, and more blocks are possibly buried under mature regolith. An overall blocky interior is perhaps largely responsible for the circular polarization ratios (CPR) enhancement observed earlier for Shackleton (Nozette et al. 1996; Simpson & Tyler 1999).

4. CONCLUSION

In this study, we evaluate previous hypotheses about the distinctive relative reflectance of Shackleton crater's interior, as reported from the Clementine (Nozette et al. 1996), LRO (Zuber et al. 2012), and Kaguya (Haruyama et al. 2008) missions, using high-resolution PSR images and topography from ShadowCam. We confirm the occurrence of near-continuous mass wasting, as hypothesized by Haruyama et al. (2013) and Zuber et al. (2012), based on flowline signatures observed from images of the permanently shadowed interior walls. ShadowCam images show that small craters (D < 30 m) are sparse on the inner walls, suggesting that debris flows occur both frequently and episodically. Previous studies point out that wall slopes near the angle of repose lead to the exposure of high reflectance underlying material. We confirm this, but add from ShadowCam DTMs that at small pixel scales (12 m), particularly on wall scarps, much steeper slopes exist (39° at 99th percentile). These extreme slopes cause instability in the walls, as shown by our computations, resulting in periodic mass wasting. These events are primarily characterized by dry, sweeping granular flows whose flowlines are visible in ShadowCam images, overlapping with block-fall tracks. Over time, these granular flows significantly alter the topography, creating distinct convergence patterns observable in horizontal curvature maps. The combination of ShadowCam images and topographical data confirms that significant landslides have occurred in the past, likely triggered by nearby impacts. Further, the ShadowCam images reveal a rocky interior in Shackleton, likely resulting from frequent debris flows and contributing significantly to the elevated radar brightness observed in the area.

Our work independently uses M^3 observations to confirm the presence of crystalline plagioclase near the permanent shadow boundary, consistent with the earlier observations of pure anorthosite (Yamamoto et al. 2012). Here, we extend the previous findings to within the permanently shadowed walls, comparing ShadowCam images with M^3 observations. We demonstrate that the plagioclase-rich rim and walls serve as a high-albedo source material, which is then intermittently exposed due to the extreme slopes. We rule out the hypothesis that the anomalously high reflectance inside Shackleton is due to the presence of ice or frost (Zuber et al. 2012). Our analysis of over 200 ShadowCam images of the wall and floor does not show any clear evidence of surface ice or frost (supporting with visual

evidence the discussions in Haruyama et al. 2008). Overall, ShadowCam observations synthesize previous hypotheses about Shackleton, and we conclude that the relatively high reflectance within the Shackleton PSR is due to the continued exposure of plagioclase-rich material, rather than water ice or frost.

Our work also explains the observation (Lucey et al. 2014) that the floor of Shackleton is relatively brighter than other nearby craters. The floor of Shackleton crater is predominantly covered with mature regolith that exhibits lower reflectance than the surrounding walls. However, compared to the floors of nearby craters, Shackleton's floor exhibits higher reflectance because of the continual admixing of high albedo material from the walls onto the floor.

We also propose that Shackleton Crater is younger than its commonly assigned Imbrian age of more than 3.4 billion yr (Spudis et al. 2008; Zuber et al. 2012; Tye et al. 2015; Kring et al. 2021). This hypothesis is based on our observations of very steep wall slopes and mass wasting features in the Shackleton crater, which are typical of Copernican and Eratosthenian craters. Our hypothesis is consistent with recent analysis (Giuri et al. 2024), suggesting that Shackleton may have formed as early as the mid-Eratosthenian period (~2.5 Ga).

ACKNOWLEDGMENTS

The authors gratefully acknowledge the work of ShadowCam, LROC, and LOLA operations personnel who made it possible to acquire high-resolution data. The authors also thank the KPLO operations personnel for their support in acquiring ShadowCam stereo observations. The National Aeronautics and Space Administration Lunar Reconnaissance Orbiter and ShadowCam projects supported this work.

ORCIDs

Prasun Mahanti https://orcid.org/0000-0003-0805-8074
Shuai Li https://orcid.org/0000-0002-9885-0809
Mark S. Robinson https://orcid.org/0000-0001-9964-2932
Thomas Watters https://orcid.org/0000-0001-6756-6066
Paul Lucey https://orcid.org/0000-0002-4959-2495
Brad Jolliff https://orcid.org/0000-0002-8294-4501
Madeleine Manheim https://orcid.org/0000-0002-1678-0481
Cordell Michaud https://orcid.org/0009-0000-6568-9230

REFERENCES

Barker MK, Mazarico E, Neumann GA, Smith DE, Zuber MT, et al., A new view of the lunar south pole from the lunar orbiter laser altimeter (LOLA), Planet. Sci. J. 4, 183 (2023). https://doi.org/10.3847/PSJ/acf3e1

Barker MK, Mazarico E, Neumann GA, Smith DE, Zuber MT, et al., Improved lola elevation maps for south pole landing sites: error estimates and their impact on illumination conditions, Planet. Space Sci. 203, 105119 (2021). https://doi.org/10.1016/j.pss.2020.105119

Barker MK, Mazarico E, Neumann GA, Zuber MT, Haruyama J, et al., A new lunar digital elevation model from the lunar orbiter laser altimeter and Selene terrain camera, Icarus, 273, 346-355 (2016). https://doi.org/10.1016/j.icarus.2015.07.039

Carrier WD III, Olhoeft GR, Mendell W, Physical properties of the lunar surface. in Lunar Sourcebook: A User's Guide to the Moon, Heiken G, Vaniman D, French BM, eds. (Cambridge University Press, Cambridge, 1991). 475-594.

Cheek LC, Hanna KLD, Pieters C, Head JW, Whitten JL, The distribution and purity of anorthosite across the orientale basin: new perspectives from moon mineralogy mapper data, J. Geophys. Res. Planet. 118, 1805-1820 (2013). https://doi.org/10.1002/jgre.20126

Cheek LC, Pieters CM, Reflectance spectroscopy of plagioclase-dominated mineral mixtures: Implications for characterizing lunar anorthosites remotely, Am. Mineral. 99, 1871-1892 (2014). https://doi.org/10.2138/am-2015-5077CCBYNCND

Feldman WC, Lawrence DJ, Elphic RC, Barraclough BL, Maurice S, et al., Polar hydrogen deposits on the moon, J. Geophys. Res. Planet. 105, 4175-4195 (2000). https://doi.org/10.1029/1999JE001129

Gallen SF, Clark MK, Godt JW,Coseismic landslides reveal near-surface rock strength in a high-relief, tectonically active setting, Geology, 43, 11-14 (2015). https://doi.org/10.1130/G36080.1

Gawronska AJ, Barrett N, Boazman SJ, Gilmour CM, Halim SH, et al., Geologic context and potential eva targets at the lunar south pole, Adv. Space Res. 66 (6), 1247-1264 (2020). https://doi.org/10.1016/j.asr.2020.05.035

Gertsch L, Gustafson R, Gertsch R. Effect of water ice content on excavatability of lunar regolith, in Aip conference proceedings, vol. 813 (American Institute of Physics, Albuquerque, 2006), 1093-1100.

Giuri B, Van der Bogert CH, Robinson MS, Hiesinger H, Multiple impact sources for light plains around the lunar south pole, J. Geophys. Res. Planet. 129, e2024JE008605 (2024). https://doi.org/10.1029/2024JE008605

Hanna KLD, Cheek LC, Pieters CM, Mustard JF, Greenhagen BT, et al., Global assessment of pure crystalline plagioclase

across the Moon and implications for the evolution of the primary crust, J. Geophys. Res. Planets, 119, 1516-1545 (2014). https://doi.org/10.1002/2013JE004476

Haruyama J, Ohtake M, Matsunaga T, Morota T, Honda C, et al., Lack of exposed ice inside lunar south pole Shackleton crater, Science, 322, 938-939 (2008). https://doi.org/10.1126/science.1164020

Haruyama J, Yamamoto S, Yokota Y, Ohtake M, Matsunaga T, An explanation of bright areas inside Shackleton Crater at the lunar south pole other than water-ice deposits, Geophys. Res. Lett. 40, 3814-3818 (2013). https://doi.org/10.1002/grl.50753

Henriksen MR, Manheim MR, Burns KN, Seymour P, Speyerer EJ, et al., Extracting accurate and precise topography from LROC narrow-angle camera stereo observations, Icarus, 283, 122-137 (2017). https://doi.org/10.1016/j.icarus.2016.05.012

Humm DC, Kinczyk MJ, Brylow SM, Wagner RV, Speyerer EJ, et al., Calibration of shadowcam, J. Astron. Space Sci. 40, 173-197 (2023). https://doi.org/10.5140/JASS.2023.40.4.173

Jaeger HM, Liu C, Nagel SR, Relaxation at the angle of repose, Phys. Rev. Lett. 62, 40-43 (1989). https://doi.org/10.1103/PhysRevLett.62.40

Kokelaar BP, Bahia RS, Joy KH, Viroulet S, Gray JMNT, Granular avalanches on the moon: mass-wasting conditions, processes, and features, J. Geophys. Res. Planet. 122, 1893-1925 (2017). https://doi.org/10.1002/2017JE005320

Krcho J, Teoretická concepcia a interdisciplinárne aplikácie komplexného digitálneho modelu reliéfu pri modelovan¨ı dvojdimenzionálnych poli, Geografický Časopis, 35, 265-291 (1983).

Kreslavsky MA, Head JW, The steepest slopes on the moon from lunar orbiter laser altimeter (lola) data: Spatial distribution and correlation with geologic features, Icarus, 273, 329-336 (2016). https://doi.org/10.1016/j.icarus.2016.02.036

Kring DA, Kramer GY, Bussey DBJ, Hurley DM, Stickle AM, et al., Prominent volcanic source of volatiles in the south polar region of the Moon, Adv. Space Res. 68, 4691-4701 (2021). https://doi.org/10.1016/j.asr.2021.09.008

Li S, Lucey PG, Milliken RE, Hayne PO, Fisher E, et al., Direct evidence of surface-exposed water ice in the lunar polar regions, Proc. Natl. Acad. Sci. 115, 8907-8912 (2018). https://doi.org/10.1073/pnas.1802345115

Li S, Milliken RE, An empirical thermal correction model for Moon Mineralogy Mapper data constrained by laboratory spectra and Diviner temperatures, J. Geophys. Res. Planet. 121, 2081-2107 (2016). https://doi.org/10.1002/2016JE005035

Li S, Moriarty DP III, Pieters CM, Klima RL, Dapremont AM, A controlled mosaic of Moon Mineralogy Mapper (M^3) reflectance data in the lunar polar regions for understanding the mineralogy and water of the Artemis exploration zone, Icarus, 440, 116668 (2025). https://doi.org/10.1016/j.icarus.2025.116668

Lucey PG, Neumann GA, Riner MA, Mazarico E, Smith DE, et al., The global albedo of the moon at 1064 nm from lola, J. Geophys. Res. Planet. 119, 1665-1679 (2014). https://doi.org/10.1002/2013JE004592

Mahanti P, Robinson MS, Humm DC, Wagner RV, Estes NM, et al., Preliminary characterization of secondary illumination at shackleton crater permanently shadowed region from ShadowCam observations and modeling. J. Astron. Space Sci. 40, 131-148 (2023). https://doi.org/10.5140/JASS.2023.40.4.131

Manheim M, Henriksen M, Wagner R, Michaud C, the ShadowCam Team, ShadowCam digital terrain models of permanently shadowed regions, Proceedings of the 55th Lunar and Planetary Science Conference, The Woodlands, TX, 11-15 Mar 2024.

Mishra A, Kumar PS, Spatial and temporal distribution of lobate scarps in the lunar south polar region: Evidence for latitudinal variation of scarp geometry, kinematics and formation ages, neo-tectonic activity and sources of potential seismic risks at the artemis candidate landing regions, Geophys. Res. Lett. 49, e2022GL098505 (2022). https://doi.org/10.1029/2022GL098505

Mitchell JK, Houston WN, Scott RF, Costes NC, Carrier WD III, et al., Mechanical properties of lunar soil: density, porosity, cohesion and angle of internal friction, vol. 3, Proceedings of the Lunar Science Conference (Pergamon Press, Oxford, UK, 1972).

Mitusov AV, Stark A, Khrisanov VR, Oberst J, Hidden morphology of Shackleton crater, lunar south pole, Planet. Space Sci. 238, 105795 (2023). https://doi.org/10.1016/j.pss.2023.105795

Newmark NM, Effects of earthquakes on dams and embankments, Geotechnique. 15, 139-160 (1965). https://doi.org/10.1680/geot.1965.15.2.139

Nozette S, Lichtenberg CL, Spudis P, Bonner R, Ort W, et al., The clementine bistatic radar experiment, Science. 274, 1495-1498 (1996). https://doi.org/10.1126/science.274.5292.1495

Ohtake M, Haruyama J, Matsunaga T, Yokota Y, Morota T, et al., Performance and scientific objectives of the selene (kaguya) multiband imager, Earth Planets Space. 60, 257-264 (2008). https://doi.org/10.1186/BF03352789

Ohtake M, Matsunaga T, Haruyama J, Yokota Y, Morota T, et al., The global distribution of pure anorthosite on the moon, Nature. 461, 236-240 (2009). https://doi.org/10.1038/nature08317

Robinson MS, Brylow SM, Caplinger MA, Carter LM, Clark MJ, et al., ShadowCam Instrument and Investigation Overview. J. Astron. Space Sci. 40, 149-171 (2023). https://doi.org/

10.5140/JASS.2023.40.4.149

Robinson MS, Brylow SM, Tschimmel M, Humm D, Lawrence SJ, et al., Lunar reconnaissance orbiter camera (LROC) instrument overview, Space Sci. Rev. 150, 81-124 (2010). https://doi.org/10.1007/s11214-010-9634-2

Shary PA, Sharaya LS, Mitusov AV, Fundamental quantitative methods of land surface analysis, Geoderma. 107, 1-32 (2002). https://doi.org/10.1016/S0016-7061(01)00136-7

Simpson RA, Tyler GL, Reanalysis of clementine bistatic radar data from the lunar south pole, J. Geophys. Res. Planets. 104, 3845-3862 (1999). https://doi.org/10.1029/1998JE900038

Spudis PD, Bussey B, Plescia J, Josset JL, Beauvivre S, Geology of Shackleton crater and the South pole of the Moon, Geophys. Res. Lett. 35, L034468 (2008). https://doi.org/10.1029/2008GL034468

Thomson BJ, Bussey DBJ, Neish CD, Cahill JTS, Heggy E, et al., An upper limit for ice in Shackleton crater as revealed by LRO mini-RF orbital radar, Geophys. Res. Lett. 39, L052119 (2012). https://doi.org/10.1029/2012GL052119

Tye AR, Fassett CI, Head JW, Mazarico E, Basilevsky AT, et al., The age of lunar South circumpolar craters Haworth, Shoemaker, Faustini, and Shackleton: implications for regional geology, surface processes, and volatile sequestration, Icarus. 255, 70-77 (2015). https://doi.org/10.1016/j.icarus.2015.03.016

Watters TR, Schmerr NC, Weber RC, Johnson CL, Speyerer EJ, et al., Tectonics and seismicity of the lunar South polar region, Planet. Sci. J. 5, 22 (2024). https://doi.org/10.3847/PSJ/ad1332

Watters TR, Speyerer EJ, Robinson MS, Recent landslides and their relation to young thrust fault scarps on the moon, in 53rd Lunar and Planetary Science Conference, The Woodlands, TX, 7-11 Mar 2022.

Xiao Z, Zeng Z, Ding N, Molaro J, Mass wasting features on the moon: how active is the lunar surface? Earth Planet. Sci. Lett. 376, 1-11 (2013). https://doi.org/10.1016/j.epsl.2013.06.015

Yamamoto S, Nakamura R, Matsunaga T, Ogawa Y, Ishihara Y, et al., Massive layer of pure anorthosite on the moon, Geophys. Res. Lett. 39, L052098 (2012). https://doi.org/10.1029/2012GL052098

Zuber MT, Head JW, Smith DE, Neumann GA, Mazarico E, et al., Constraints on the volatile distribution within Shackleton crater at the lunar South pole. Nature. 486, 378-381 (2012). https://doi.org/10.1038/nature11216

APPENDIX 1.

ShadowCam Images and ShadowCam DTMs

The ShadowCam team creates digital terrain models at 6-7 m/pixel using images that were targeted for geo stereo (Manheim et al. 2024). These images are acquired on close-to-successive orbits to ensure similar lighting conditions between images. Typical stereo sets consist of a nadir image and a ~20° pitch slew. The Shackleton DTM and mosaic used here was produced using nine images (five nadirs: M043503903S, M043475618S, M043461476S, M043532189S, M043503903S, and four pitch slews: M043482711S, M043468570S, M043454432S, M043525136S, M043510996S) that were acquired on December 21, 2023, during the lunar south pole summer. In addition to these 9 images, two observations M081161776S and M084203041S acquired at 1 m/pixel scale were used. ShadowCam DTMs are produced using SOCET SET 5.5.0, a commercial software from BAE Systems, and USGS ISIS, using the methods outlined in Henriksen et al. (2017). They are controlled to the best available LOLA track dataset; in this case, the LOLA point cloud LDEM 80S ADJ. XYZI (Barker et al. 2023). DTMs are extracted at ~3 times the pixel scale of the stereo images. The ShadowCam team releases derived products, including DTMs, on a three-month schedule; products are to become available about one year after the images used to create the products were acquired. ShadowCam data products are available from the PDS (https://pds.shadowcam.im-ldi.com/).

APPENDIX 2.

Directionality Description

To discuss direction, we use the convention near/far/trailing/leading for up/down/right/left respectively in a standard south polar stereographic projection (Fig. A1). In this description near (up) indicates towards Earth, far (down) indicates away from Earth, leading (left) indicates the leading hemisphere of the Moon and trailing (right) indicates the trailing hemisphere of the Moon. The corresponding walls of Shackleton are also marked as near/far/trailing/leading. Consequently, a combination of near/far and leading/trailing can be used to describe directions in between. For example, far-trailing wall indicates the wall region between the trailing and far walls.

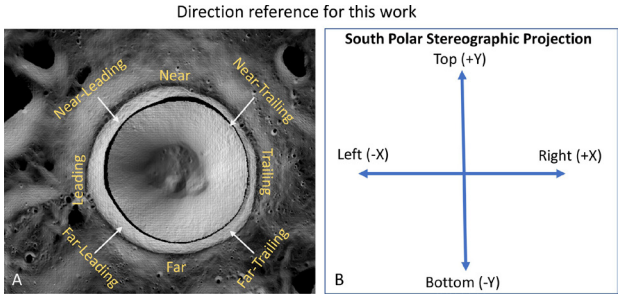

Fig. A1. Visual direction reference for this work.

APPENDIX 3.

Polar Maps of Crystalline Plagioclase from M^3 data

The crystalline plagioclase is mapped from a controlled mosaic of M^3 data near the lunar south pole. The M^3 data were first thermally corrected using the method in (Li & Milliken, 2016). We used the maximum median reflectance value for a pixel with multiple repeat observations, which could help to exclude observations in shadow. However, if all repeat observations were in shadow, we defined such regions are not covered by M^3. Due to the degraded signal-to-noise ratio (SNR) of M^3 data in the polar regions, we used a smoothness threshold developed in the study of (Li et al. 2025) to rule out noisy pixels in our mosaic. M^3 data in OP1A, 1B, and 2A were acquired when the star-tracker still worked and were preferentially used in our mosaic to ensure the accurate spatial registration of the final mosaic products. M^3 data in those three OPs covers around 65% of the polar regions. We manually picked M^3 image cubes from OP2B (140 m/pixel) and OP2C (280 m/pixel) that match best (e.g., least registration offset) with the commonly used LOLA digital elevation model (DEM) product SLDEM2015 (60 m/pixel; Barker et al., 2016) to fill the remaining around 35% gaps. The high sampling density of M^3 data near the poles allows us to derive a polar mosaic of M^3 data at 140 m/pixel (Li et al. 2025).

APPENDIX 4.

Unstable Slope Locations on the Shackleton Topography

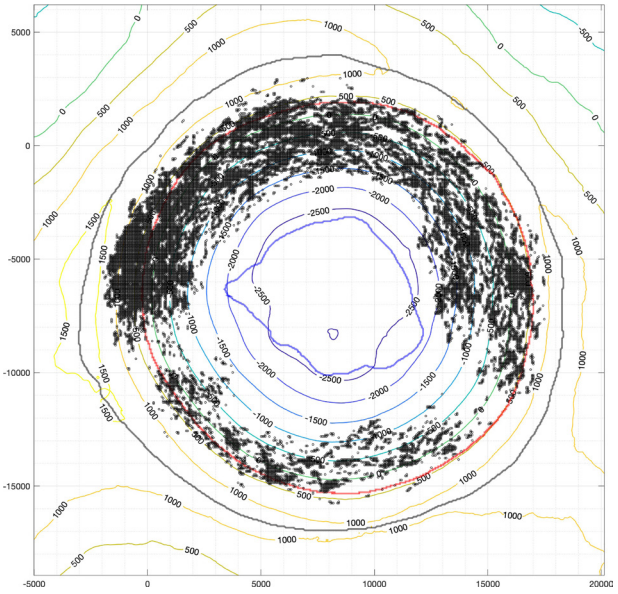

Fig. A2. Visualization of locations (black dots) with slope values 32° or higher for outcrops and are unstable from our analysis. Apart from the elevation contours (marked with numbers), the figure also shows Shackleton's rim (black), PSR boundary (red), and floor boundary (blue) used in this work. Map in polar stereographic projection. X and Y axis are distance in meters from south pole.